Proceedings of the Seventh International Conference on
Railway Technology: Research, Development and Maintenance
Edited by: J. Pombo
Civil-Comp Conferences, Volume 15, Paper 12.3
Civil-Comp Press, Edinburgh, United Kingdom, 2026
ISSN: 2753-3239, doi: 10.4203/ccc.15.12.3

Ballast Volume Assessment for Ballasted Railways Based on Mobile Laser Scanning System

H. Xu[1], Q. Mao[1,2], K. Zhang[3], Y. Shi[1,4], T. Wang[1], Y. Mu[2] and G. Wang[1]

[1]School of Remote Sensing and Information Engineering, Wuhan University, China
[2]Hubei luojia laboratory, Wuhan, China
[3]Wuhan Hanning Rail Transit Technology Corporation Limited, China
[4]State Key Laboratory of Rail Transit Vehicle System, Southwest Jiaotong University, China

Abstract

This paper proposes a method for evaluating ballast volume on ballasted railway using a mobile laser scanning system. To address volumetric measurement tasks in dynamic environments, a reversed clothing simulation filtering is employed to extract the cross-sections of track bed. A decision-tree-driven method is further developed to identify the design ballast bed sections. Iterative closest point method is used to align the measured cross-sections with the design cross-sections based on the matched rails. An evaluation framework incorporating confidence intervals from adjacent cross-sections is established, enabling accurate and robust estimation of ballast volume. Experimental results demonstrate that the proposed method achieves a relative measurement accuracy better than 4.04%, with a maximum deviation of only 2.68% in volume estimation. Data acquisition can be performed under dynamic conditions with a mobile platform operating at speeds of 2-10 km/h, while maintaining a relative accuracy better than 5%. The proposed approach enables high-precision mobile measurement based on an electrically powered platform and a scanning system, significantly improving both accuracy and stability in ballast volume assessment.

Keywords: ballasted railway, ballast volume, mobile measurement, mobile laser scanning, point cloud, volume computation.

1 Introduction

As the backbone of railway transportation networks, ballasted railways are widely used worldwide, accounting for more than 85% of the railway network in the United

States and approximately 70% in China [1]. A ballasted railway consists of key components including rails, sleepers, ballast, and fastening systems, which jointly support train operations [2]. Under train loads, interactions among ballast particles transfer and distribute vertical stresses to the subgrade, while attenuating lateral shear forces and vibration energy, and facilitating drainage [3,4]. However, long-term cyclic loading alters the stress state within the ballast layer, leading to redistribution of surface ballast and degradation of deeper ballast layers [5]. These changes can adversely affect track geometry and may even pose significant risks to operational safety. Therefore, periodic and comprehensive inspection of the ballasted track bed is essential to evaluate key condition parameters, including ballast volume deficiency or excess, particle size and gradation, thereby providing reliable information for timely maintenance of ballasted railways [6].

Inspection methods for assessing ballast conditions in ballasted railways have continuously evolved with advances in sensing technologies. Hammer sounding [7], fixed sensors [8], and Ground-penetrating radar (GPR) [9,10] were widely used. In contrast, three-dimensional laser scanning technology provides active sensing capabilities, can operate flexibly within limited maintenance time windows, and is less affected by highly reflective targets. Moreover, the acquired point clouds allow direct measurement of geometric parameters [11]. Mobile laser scanning (MLS) systems, with the LiDAR as the core component, can achieve high inspection speeds, making them well suited for rapid acquisition of ballast data and subsequent condition assessment within limited time.

Zarembski et al. [12] employed the BallastSaver ballast profile inspection vehicle developed by GREX to measure ballast deficiency. The system operates at speeds ranging from 1 to 20 mph, with cross-sectional spacing varying from 9 mm to 178 mm. However, the ballast volume was estimated by simply multiplying the spacing between adjacent cross-sections by the deficiency area within each section, resulting in relatively large computational errors.Sadeghi et al. [13] proposed a ballast layer geometry index (BLGI) that integrates both ballast deficiency and excess. Detailed values were computed using a similar approach, and 10 cm * 10 cm maps were generated to indicate areas of insufficient and excessive ballast. Lesiak et al. [14] utilized an inspection vehicle developed by Mermec, equipped with the V-CUBE universal laser and camera system, to acquire images of the track bed and investigate vegetation intrusion. Aldao et al. [15] proposed a railway ballast scanning approach based on the solid-state LiDAR system LiVOX Avia. The acquired point clouds were compared with high-density ground points obtained using the Faro Focus 3D scanner. The results demonstrated that the LiVOX system can distinguish single-layer ballast displacements with particle diameters ranging from 2.5 cm to 5 cm. Luo et al. [16] developed a ballast scanning vehicle (BSV), whose core sensors include line-scan cameras, area-array cameras, and a three-dimensional scanner. Image segmentation techniques based on Swin Transformer and Cascade R-CNN were employed to evaluate the percentage of degraded ballast (PDS) and fouling indices. Bojarczak et al. [17] used a laser triangulation system to acquire line-scan images of ballast regions. Sleepers were segmented using Mask R-CNN and YOLACT, and ballast unevenness was assessed according to Polish railway standards.

For large-scale railway inspection tasks involving ballast condition assessment, MLS-based estimation methods still face two major challenges. First, existing studies do not adequately account for the adaptability of ballast bed profiles; the lack of a unified reference across different types of track bed cross-sections prevents ballast volume estimation from accurately reflecting real conditions. Second, multiple factors—including the scanner triggering frequency of the MLS system, the speed of the mobile platform, cross-sectional spacing, and the volume estimation strategy—can all influence ballast condition measurements. To date, systematic and quantitative analyses of these factors remain limited.

To address the aforementioned issues, this study proposes a comprehensive solution. First, track bed cross-sections are extracted using a reverse clothing simulation filtering (CSF) method. Subsequently, a decision tree–driven approach is developed to identify ballast bed profiles. Guided by railway inventory data, corresponding design cross-sections are generated for ballast volume estimation. Next, leveraging the unique correspondence of rail positions between the measured and design cross-sections, an ICP-based registration method is proposed to align the sections. Finally, with practical applications in mind, confidence intervals for ballast volume are introduced to provide a reliable basis for ballast maintenance decisions. Data acquisition is conducted using a Pro 360 cross-sectional scanner mounted on a self-developed electrically powered inspection platform [18, 19]. By controlling the acquisition frequency and platform speed, the influence of these factors on ballast condition assessment is quantitatively analyzed.

2 Methods

2.1 Track bed extraction

According to the principles of MLS, a cross-sectional scanner acquires three-dimensional coordinates and attribute information of surrounding targets during each full rotation. As the mobile platform moves forward, point clouds of the entire surveyed area are progressively generated. Consequently, MLS point clouds can be organized into helical scan lines based on acquisition time, where each scan line corresponds to a spatial cross-section. Given that laser scanners can acquire hundreds of thousands of points per second, the resulting point cloud along a railway line is extremely large. Moreover, since the scanner is mounted on a mobile platform constrained by the rails, the vertical line passing through the scanner's optical center is theoretically aligned with the rail centerline. Therefore, prior to further processing, a pass-through filter is applied to remove all points located more than 6 m from both sides of the scanner, resulting in the raw input point cloud shown in Fig. 1(a).

In the railway scenario described above, a single cross-section along the track direction contains relevant targets such as rails, sleepers, and the track bed, which are marked with green rectangles, as well as non-relevant objects including the catenary system, cantilever structures, and vegetation, highlighted with red rectangles. Based on the spatial distribution characteristics of these relevant targets, a reverse cloth simulation filtering method is proposed to extract track bed cross-sections.

CSF is a widely used algorithm in point cloud processing for ground surface extraction. It assumes that a piece of cloth falls under gravity from above, and the final resting surface represents the underlying terrain. However, for the scene point cloud shown in Fig. 1(a), when the cloth falls from above, non-target structures preventing complete extraction of the track bed cross-section. To address this issue, the Z-axis values of the scene are inverted. Under this transformation, the cloth effectively falls from above relative to the inverted geometry, enabling accurate extraction of the track bed cross-section, as illustrated in Fig. 1(b).

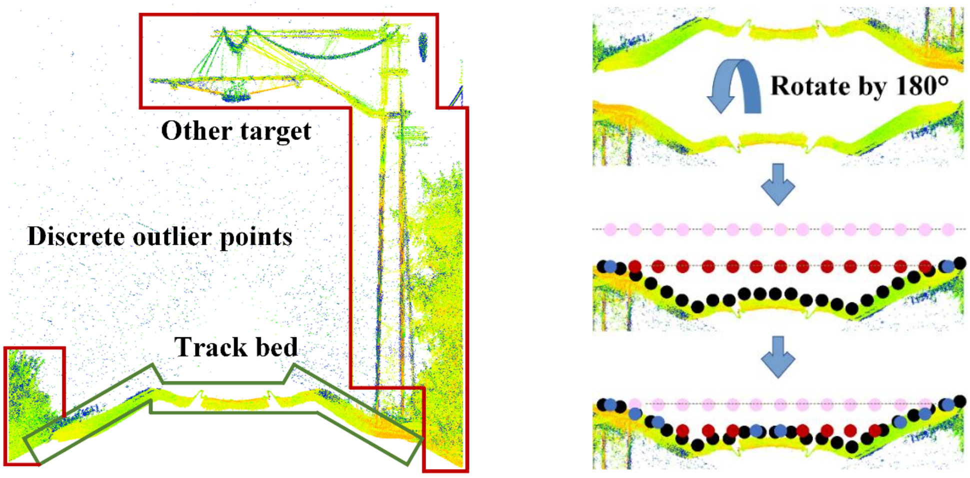

(a) (b) Extraction of track bed

Figure 1: Schematic diagram of track bed cross-section extraction. (a) Original input point cloud; (b) Extraction of track bed cross-section based on CSF.

For the input point cloud at chainage k, denoted as $\boldsymbol{P}_{k,\text{in}}$, each point $(X_{k,\text{in}}, Y_{k,\text{in}}, Z_{k,\text{in}}) \epsilon \boldsymbol{P}_{k,\text{in}}$ is transformed by inverting its Z-coordinate, yielding $(X_{k,\text{in}}, Y_{k,\text{in}}, -Z_{k,\text{in}})$, which serves as the input to the CSF algorithm. Assuming a cloth surface C_f, the position of each cloth particle at time t is denoted by $X_C(t)$. The external force due to gravity is represented as $F_{\text{ext}}(X_C, t)$, while the internal forces arising from interactions among cloth particles are denoted as $F_{\text{int}}(X_C, t)$. The temporal evolution of the cloth particle positions is then governed by Eq. (1).

$$m \frac{\partial X_C(t)}{\partial t^2} = F_{\text{ext}}(X_C, t) + F_{\text{int}}(X_C, t) \tag{1}$$

Figure 1(b) illustrates the process of cloth falling until the track bed cross-section is obtained. In the figure, pink points denote the previous state of cloth particles, red points indicate their current state, blue points represent particles that have become fixed, and black points correspond to the theoretical track bed surface.

Step 1: Initialization. A virtual cloth is placed above the inverted point cloud.

Step 2: Particle displacement is computed under the effect of gravity according to Eq. (1), during which some particles may move below the ground surface. Light red points indicate the previous positions of the particles.

Step 3: Collision detection. The updated particle positions are checked to determine whether they have reached the ground surface; once a particle reaches the surface, it is fixed and no longer allowed to move. Blue points represent such fixed particles.

Step 4: Internal force update. For the remaining movable particles, their positions are updated based on the internal forces exerted by neighboring particles within the cloth.

Once all cloth particles become fixed, the track bed cross-section is delineated based on the distances between the point cloud and the corresponding cloth surface. The extracted track bed cross-section points are denoted as $\boldsymbol{P}_{k,f}$.

2.2 Ballast bed profile identification

According to standards adopted in different countries and regions, the track bed cross-section is typically divided into four components: the sleeper zone, ballast shoulder, side slope, and deep layer. Since mobile measurement systems are unable to capture data from the deep layer, the design cross-section can be used as a reference when estimating ballast volume deficiency and excess. The design cross-section varies with factors such as railway line type, design speed, and sleeper type, particularly in parameters including the central depth beneath the rail, ballast shoulder height, and side slope ratio. To improve the level of automation, a decision tree–based approach is proposed to automatically match the design cross-section at any chainage using railway inventory data.

Taking conventional railways in China as an example, Fig. 2(a) presents the decision tree for selecting the design cross-section used in ballast volume estimation for light mixed-traffic railway lines, while Fig. 2(b) shows the corresponding decision tree for intercity mixed-traffic railway lines.

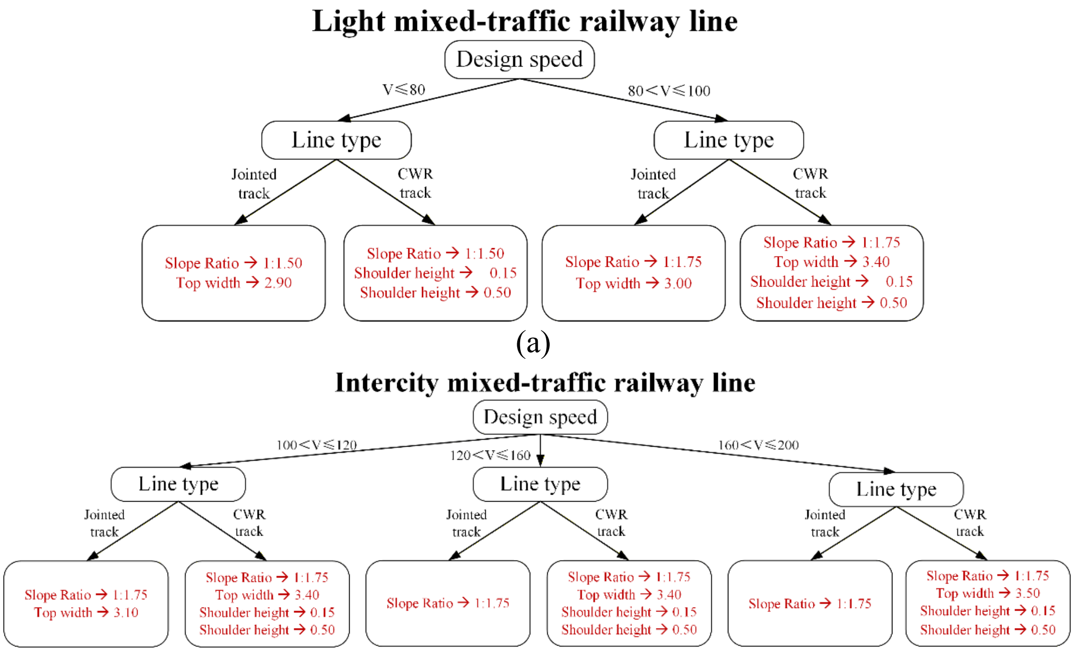

Figure 2: Schematic diagram of decision tree. (a) Decision tree of light mixed-traffic railway line; (b) Decision tree of intercity mixed-traffic railway line.

The decision tree shown in Fig. 2 corresponds only to light mixed-traffic railway lines on main lines. Additional decision trees are defined for intercity mixed-traffic railways, high-speed railways, and heavy-haul railways, as well as for station tracks, including arrival–departure tracks, shunting tracks, and other yard tracks. For any other types of design cross-sections, the corresponding information can be obtained from the railway inventory data of the inspected line.

Each decision outcome corresponds to a unique track bed cross-section, which may either include or exclude sleepers. The discretized point clouds for these two cases are denoted as $\boldsymbol{P}_{s,\text{design}}$ and $\boldsymbol{P}_{n,\text{design}}$, respectively.

2.3 Rail-based cross-section registration

For the track bed cross-section point cloud $\boldsymbol{P}_{k,f}$ obtained in Section 2.1, there exists a unique corresponding discretized design cross-section point cloud, either $\boldsymbol{P}_{s,\text{design}}$ or $\boldsymbol{P}_{n,\text{design}}$. Within the cross-section, the rails exhibit strong continuity and, compared with sleepers and side slopes, are less prone to deformation, making them a stable and salient common feature. By registering the rail segments in the measured point cloud with those in the design cross-section, a unified coordinate reference can be established for subsequent evaluation of ballast conditions within the current section.

To determine whether the current cross-section contains sleepers, MLS point clouds within a certain longitudinal range are projected onto an image plane, and the centers of sleepers are detected using a YOLO v8-based network. Let the grid size in the image be G, and the width of the track bed be W. The number of pixels in the direction perpendicular to the track is then given by $N = \text{ceil}(W/G)$, where $\text{ceil}(\cdot)$ denotes the ceiling function. For simplicity, all pixels are assumed to be square. The original XOY coordinates of the point cloud are replaced by pixel coordinates, and the pixel intensity values correspond to the reflectance of the targets. The projection relationship is defined as follows.

$$\begin{cases} X = \text{ceil}((x_i - x_{\min})/G) \\ Y = \text{ceil}((y_i - y_{\min})/G) \\ V_p = I_i \end{cases} \tag{2}$$

where (X, Y) denote the pixel coordinates in the projected image, and V_p represents the pixel intensity value. (x_i, y_i, z_i) are the three-dimensional coordinates of the i-th point in the point cloud, while $x_{\min}$ and $y_{\min}$ denote the minimum values along the corresponding coordinate axes. I_i denotes the intensity of the i-th point. Figure 3 illustrates the projected intensity image and the extracted sleeper regions.

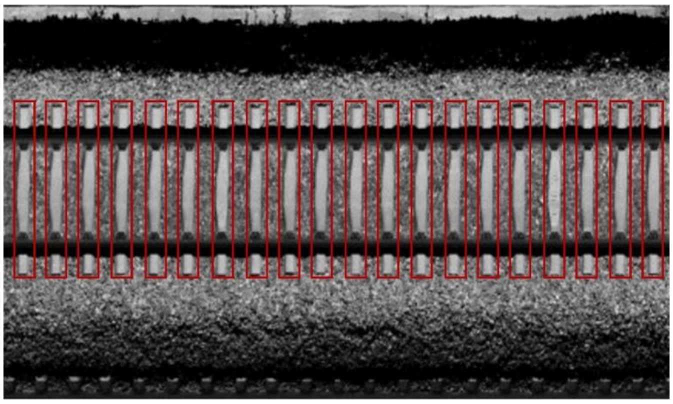

Figure 3: Intensity image generation and sleeper segmentation.

For cross-sections classified by whether sleepers are present, the iterative closest point (ICP) algorithm is employed to register the MLS-derived track bed cross-section point cloud with the corresponding design cross-section point cloud. The principle of ICP is to minimize the distance between corresponding points in the source and reference point clouds. While the standard formulation is defined for three-dimensional point clouds, the registration of rail head points within a cross-section represents a degenerate two-dimensional case. Accordingly, the matching criterion is reformulated as shown in Eq. (3).

$$\min F(\boldsymbol{R},\boldsymbol{T}) = \frac{1}{n}\sum_{i=1}^{n}\|\boldsymbol{P}_i - (\boldsymbol{R}\cdot\boldsymbol{Q}_i + \boldsymbol{T})\|^2 \tag{3}$$

where $\boldsymbol{R}$ denotes the rotation matrix, and $\boldsymbol{T}$ represents the translation vector. $\boldsymbol{P}_i$ denotes the i-th corresponding point in the reference point cloud, while $\boldsymbol{Q}_i$ denotes the i-th corresponding point in the source point cloud. n is the total number of corresponding point pairs.

2.4 Ballast condition assessment

After matching the design cross-section to each measured section, the ballast deficiency area $S_{k,q}$ and excess area $S_{k,c}$ at chainage k can be further computed. When the spacing between adjacent cross-sections is sufficiently small, the deficiency and excess areas vary smoothly with only minor differences between neighboring sections. As the spacing increases, the discrepancies between adjacent sections become more pronounced, and the corresponding ballast volume may exhibit abrupt changes. When the spacing exceeds the maximum particle size of first-grade ballast, the ballast within a cross-section can no longer be considered continuous.

Existing methods [12] and [20] estimate ballast volume by simply multiplying the cross-sectional spacing $d_{k,k+1}$ by the deficiency or excess area, which leads to inaccurate volume estimation. Considering that ballast deficiency has a more significant impact than excess in practical scenarios, this study proposes a confidence interval–based method for ballast volume estimation. For two adjacent cross-sections k and $k+1$, integration is performed using the smaller and larger area values between the two sections, respectively, to derive confidence intervals for ballast deficiency and excess volumes, denoted as $[V_{q,\min}, V_{q,\max}]$ and $[V_{c,\min}, V_{c,\max}]$.

$$\begin{cases} V_{q,\min} = \sum_{k=1}^{n-1} \min(S_{k,q}, S_{k+1,q}) \cdot d_{k,k+1} \\ V_{q,\max} = \sum_{k=1}^{n-1} \max(S_{k,q}, S_{k+1,q}) \cdot d_{k,k+1} \end{cases} \quad (4)$$

$$\begin{cases} V_{c,\min} = \sum_{k=1}^{n-1} \min(S_{k,c}, S_{k+1,c}) \cdot d_{k,k+1} \\ V_{c,\max} = \sum_{k=1}^{n-1} \max(S_{k,c}, S_{k+1,c}) \cdot d_{k,k+1} \end{cases} \quad (5)$$

In summary, by providing confidence intervals for ballast deficiency and excess, track maintenance personnel can prepare an appropriate range of ballast for replenishment, ensuring that the recommended volume is robust.

3 Results

3.1 Experimental conditions

A validation experiment was conducted at a closed test site in Wuhan, Hubei Province, China. Known volumes of ballast were placed along selected sections of a ballasted track to evaluate measurement accuracy, repeatability, and the influence of platform speed on the results. The experimental setup is shown in Fig. 4(a).

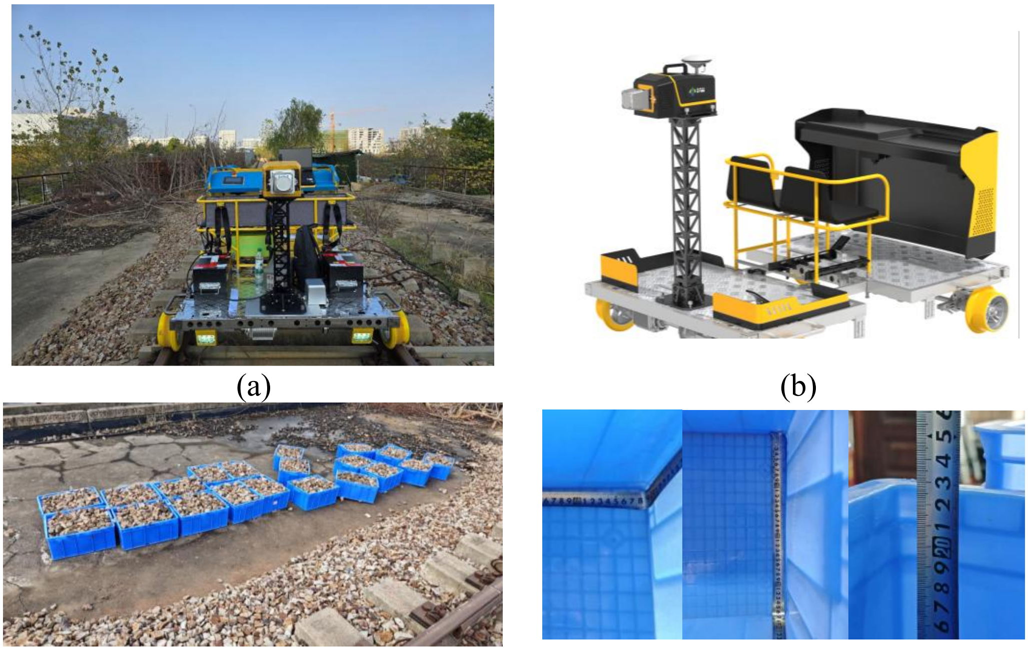

(c) (d)

Figure 4: Experimental site for technical validation. (a) Experimental site; (b) Electrically powered mobile platform and scanner; (c) Ballast container; (d) Container dimension measurement.

The mobile platform and the Pro 360 cross-sectional laser scanner were provided by Wuhan Hanning Rail Transit Technology Co., Ltd.. The integrated configuration of the electrically powered platform and the scanner is shown in Fig. 4(b), and the main system parameters are listed in Table 1.

Parameter	Metric	Parameter	Metric
Mobile platform	rMMS (cross-section)	Scanner	Pro 360
Speed	⩽20km/h	PRF	⩾1MHz
Drive mode	Electrical power	Sectional frequency	50/100/150Hz
Odometer accuracy	1mm	Ranging accuracy	⩽2mm@20m
Speed accuracy	0.03 m/s (RMS)	Angular accuracy	⩽0.01°
Time accuracy	20 ns (RMS)	Scanning angle	⩾270°

Table 1: Parameters of the mobile platform and laser scanner. (a) PRF is laser pulse repetition frequency.

The container used for validating ballast loading accuracy is shown in Fig. 4(c), with dimensions of 0.49 m * 0.37 m * 0.23 m, as illustrated in Fig. 4(d). A total of 20 containers were used, corresponding to a total ballast volume of 0.83398 m^3. After data acquisition, all data were processed on a unified workstation. The workstation is equipped with an Intel i7-14650 processor and 64 GB of memory. The proposed algorithms were implemented in C++, utilizing third-party libraries including PCL (v1.12.1), Qt (v5.14.2), OpenCV (v4.5.5), and CloudCompare.

3.2 Evaluation metrics

When ground-truth values are available, absolute evaluation metrics can be computed to quantify the deviation from the true measurements. In this study, given that the ballast volume to be added is known, the change in ballast volume before and after placement, $|V_c - V_{\mathrm{ori}}|$, should be consistent with the added ballast volume V_{in}. Accordingly, the relative measurement error of ballast volume, denoted as P_v, can be expressed by Eq. (6).

$$P_v = \frac{||V_c - V_{\mathrm{ori}}| - V_{in}|}{V_{in}} \times 100\% \tag{6}$$

where V_c denotes the estimated ballast volume after ballast placement, and V_{ori} represents the estimated ballast volume before placement.

In addition, repeated measurements were conducted over the same track section in the same direction to evaluate the internal consistency accuracy, which reflects the stability of the measurement system. The internal consistency accuracy, denoted as σ_v, is calculated according to Eq. (7).

$$\sigma_v = \sqrt{\frac{1}{m-1}\sum_{i=1}^{m}\left(V_{c,i} - \overline{V_c}\right)^2} \tag{7}$$

where m denotes the number of repeated measurements; in this study, 12 forward runs and 12 backward runs were conducted. $V_{c,i}$ represents the estimated ballast volume in the i-th measurement, and $\overline{V_c}$ denotes the mean value of the estimated ballast volume.

3.3 Measurement accuracy and stability

3.3.1 Accuracy

In this section, the mobile platform was operated at a constant speed of 4 km/h for both forward and backward runs, with the spacing between adjacent cross-sections $d_{k,k+1}$ set to 0.05 m. The original track bed point cloud was scanned three times in both directions to obtain the initial state of the track bed cross-sections. Subsequently, ballast from the containers was uniformly distributed at arbitrary locations between the two rails within the measurement section. The mobile platform then performed 12 forward and backward scans of the track bed point cloud at the same speed, resulting in a total of 30 datasets. Figure 5 presents the track bed cross-sections at the same chainage before and after ballast placement.

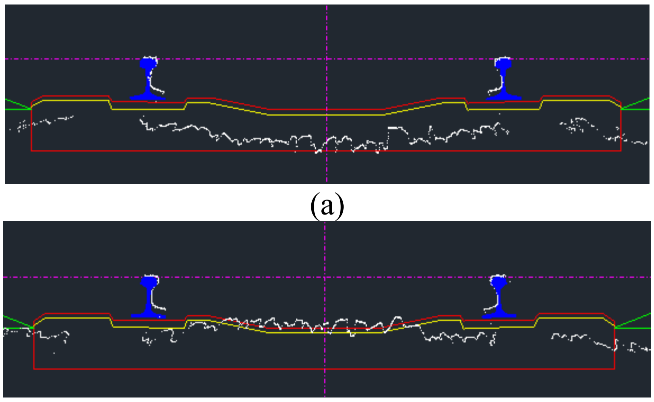

Figure 5: Comparison of track bed cross-sections before and after ballast placement. (a) Track bed cross-section before ballast placement; (b) Track bed cross-section after ballast placement.

Figure 5(a) shows the condition before ballast placement, corresponding to ballast deficiency, while Fig. 5(b) illustrates the condition after ballast placement, where excess ballast is present between the rails. The mean ballast volume obtained from six measurements prior to ballast placement was taken as the reference. The results of ballast volume change derived from 24 measurements after ballast placement are presented in Table 2.

D_{vec}	$V_c / \times 10^{-3}\mathrm{m}^3$	$P_v/\%$	$\Delta V_{c,\min}/\%$	$\Delta V_{c,\max}/\%$
0	[800.29, 847.91]	[-4.04, 1.67]	1.48	0.83
1	[812.62, 854.83]	[-2.56, 2.50]		

Table 2: Ballast volume changes before and after ballast placement.

The results indicate that, using the proposed method, the errors between the estimated ballast volume changes and the actual added ballast volume are -4.04% and 1.67% for forward runs, and -2.56% and 2.50% for backward runs, all of which are within the 5.00% measurement requirement. The discrepancies between forward and backward measurements are 1.48% for the minimum estimated volume and 0.83% for the maximum estimated volume, both satisfying the required tolerance.

To validate the superiority and accuracy of the proposed method, a comparative analysis was conducted against the approaches reported in Ref. [12] (Method 1), Ref. [20] (Method 2), and Ref. [21] (Method 3). The results are shown in Table 3.

Method	D_{vec}	$V_c/\times 10^{-3}\mathrm{m}^3$	$P_v/\%$	$\Delta V_c/\%$
1	0	865.42	3.77	4.96
	1	906.71	8.73	
2	0	854.36	2.44	5.28
	1	810.27	-2.84	
3	0	806.93	-3.24	3.79
	1	838.54	0.55	
Ours	0	824.10	-1.18	1.18
	1	833.73	0.00	

Table 3: Comparison of ballast volume estimates obtained by different methods

The results show that, after deriving the confidence interval of ballast volume using the proposed method and taking the midpoint of the interval as the estimated value, the relative measurement errors are only -1.18% and 0.00%. Compared with the most recent studies, this represents improvements of 2.06% and 0.55%, respectively. The discrepancy between forward and backward measurements is 1.18%, which is reduced by 2.61% compared with the latest methods, indicating that the proposed approach achieves the highest measurement accuracy among all methods considered.

3.3.2 Stability

Furthermore, to verify the stability of both the measurement system and the proposed method, the internal consistency accuracy of the estimated ballast volumes was calculated for each set of 12 forward and 12 backward measurements according to Eq. (7). The results are presented in Table 4.

Method	D_{vec}	$V_c/\times 10^{-3}\mathrm{m}^3$	$V_{\max}/\times 10^{-3}\mathrm{m}^3$	$\sigma_v/\times 10^{-3}\mathrm{m}^3$
1	0	865.42	69.69	35.29
	1	906.71	76.55	33.08
2	0	854.36	34.20	27.31
	1	810.27	44.43	26.70
3	0	806.93	38.25	23.54
	1	838.54	15.76	11.05
Ours	0	824.10	22.37	17.10
	1	833.73	16.64	13.53

Table 4: Comparison of measurement stability across different methods

According to Table 4, for the forward runs, the proposed method yields a maximum volume deviation of $22.37*10^{-3}$ m^3, which is $11.83*10^{-3}$ m^3 lower than that of Method

2, ranked second. The internal consistency accuracy is 17.10*10^{-3} m^3, representing a reduction of 6.44×10^{-3} m^3 compared with Method 2. For the backward runs, the maximum volume deviation is 16.64*10^{-3} m^3, and the internal consistency accuracy is 13.53*10^{-3} m^3, which are slightly higher than those of Method 3. Overall, the results demonstrate that the proposed method produces highly consistent measurements across repeated trials, with a maximum deviation of 2.68%, indicating good stability.

3.4 Influence of cross-sectional spacing on measurement results

In the validation experiments on measurement accuracy and stability, the mobile platform was operated at a constant speed of 4 km/h, and the spacing between adjacent cross-sections $d_{k,k+1}$ was set to 0.05 m. It is evident that the choice of $d_{k,k+1}$ affects both the computed ballast volume and the computational cost. To quantitatively investigate the influence of cross-sectional spacing on ballast volume estimation, a dataset from a forward run after ballast placement, whose relative error interval is entirely positive was selected. The spacing $d_{k,k+1}$ was varied from 0.01 m to 0.10 m in increments of 0.01 m. For each setting, the relative error P_v and the computational time T_v were calculated. The results are illustrated in Fig. 6.

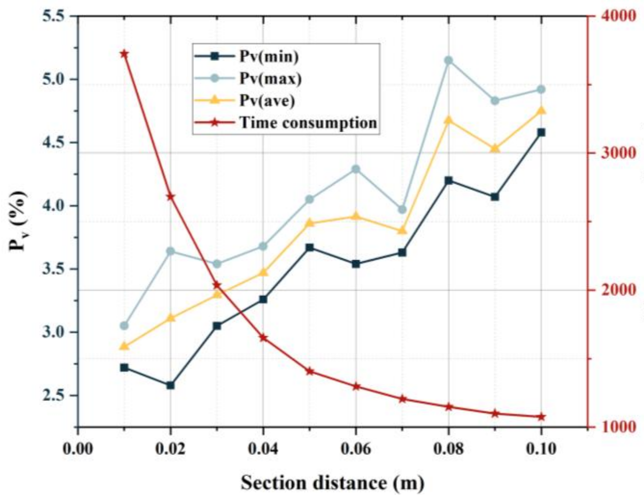

Figure 6: Effect of cross-sectional spacing on accuracy and time consumption.

The results indicate that, as the cross-sectional spacing $d_{k,k+1}$ increases, the relative error P_v of the estimated ballast volume, which are characterized by the minimum, maximum, and midpoint values of the interval exhibits an approximately linear increasing trend. It is observed that when $d_{k,k+1} \geq 0.07$m, fluctuations appear in the measurement results. This behavior can be attributed to the fact that the sampling interval becomes larger than the characteristic ballast size, leading to reduced accuracy in volume estimation. In contrast, the computational time shows a decreasing trend and gradually approaches a stable level.

3.5 Influence of platform speed on measurement results

In addition to cross-sectional spacing, the speed of the mobile platform is another key factor influencing ballast volume estimation. According to the kinematic relationship, when the platform operates at a speed of 10 km/h and the Pro 360 scanner runs at its maximum cross-sectional scanning frequency of 150 Hz, the theoretical cross-sectional spacing is 18.52*10^{-3} m. To investigate the effect of platform speed on volume estimation, the scanner frequency was fixed at 150 Hz, and data were acquired at platform speeds of 2, 4, 6, 8, and 10 km/h. With $d_{k,k+1} = 0.04$m, the resulting relative error P_v is shown in Fig. 7.

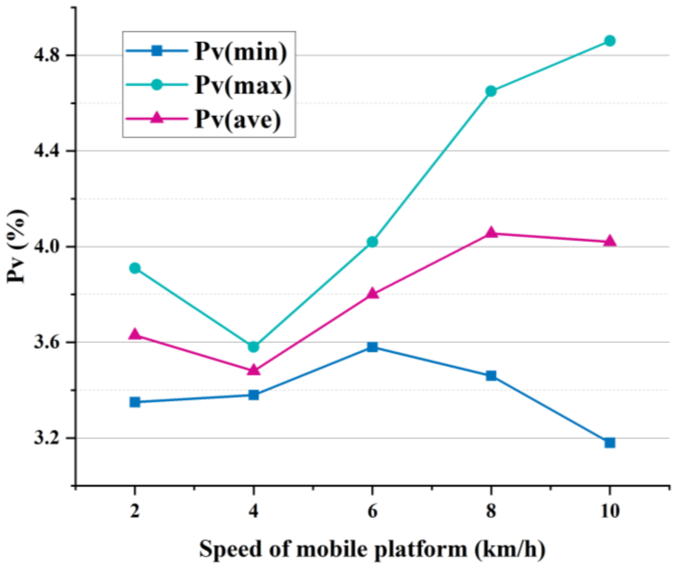

Figure 7: Effect of platform speed on accuracy.

The results indicate that, as the platform speed increases, the ballast volume estimates remain relatively stable within 6 km/h, with only minor fluctuations in the maximum and minimum estimated values. When the speed exceeds 6 km/h, the variability of both the maximum and minimum estimates becomes more pronounced. Considering that both the platform speed and the scanner frequency jointly affect the number of points involved in the computation within each cross-section, increasing the scanning frequency can improve the accuracy of ballast volume estimation under high-speed operating conditions.

4 Conclusions and Contributions

This study investigates a technical framework for applying mobile laser scanning (MLS) systems to ballast volume estimation in railway environments. Dedicated validation experiments demonstrate the effectiveness and reliability of both the measurement system and the proposed method. The main contributions of this work are summarized as follows.

(1) By integrating railway inventory data with design cross-section information, a decision tree–based approach is developed to generate the ideal track bed cross-section at a given chainage. This provides a reliable reference for matching with measured point cloud cross-sections and forms the basis for quantitative ballast volume analysis.

(2) A confidence interval–based volume estimation method is proposed, in which integration is performed using the minimum and maximum cross-sectional areas of adjacent sections. This approach improves both accuracy and stability, reducing measurement errors with respect to ground truth by 0.55% to 2.61% compared with existing methods.

(3) The effects of cross-sectional spacing and platform speed on measurement performance are systematically analyzed. Practical recommendations for selecting appropriate spacing and platform speed are provided, along with an explanation of the underlying mechanisms.

In summary, the proposed method exhibits high reliability and repeatability, enabling rapid and accurate acquisition of track bed profiles and precise estimation of ballast volume. It provides essential data support for track bed inspection and for planning ballast unloading and replenishment in ballasted railway maintenance.

Acknowledgements

This work was supported by National Natural Science Foundation of China (42501557), and China Postdoctoral Science Foundation (2023TQ0253).

References

[1] H. Cui, J. Li, Q. Hu, et al., “Real-time inspection system for ballast railway fasteners based on point cloud deep learning”, IEEE Access, 8: 61604–61614, 2019.

[2] K. Ding, J. Luo, H. Huang, et al., “I-ballast: computer vision solutions for ballast degradation analysis using deep-learning and data fusion methods”, Geodata and AI, 1: 100007, 2024.

[3] J. Xiao, L. Xue, D. Zhang, et al., “Coupled DEM-FEM methods for analyzing contact stress between railway ballast and subgrade considering real particle shape characteristic”, Computers and Geotechnics, 155: 105192, 2023.

[4] J.C.O. Nielsen, X. Li, “Railway track geometry degradation due to differential settlement of ballast/subgrade–numerical prediction by an iterative procedure”, Journal of Sound and Vibration, 412: 441–456, 2018.

[5] S. Shi, L. Gao, B. Hou, et al., “Numerical investigation on multiscale mechanical properties of ballast bed in dynamic stabilization maintenance”, Computers and Geotechnics, 144: 104649, 2022.

[6] T. Abadi, L. Le Pen, A. Zervos, et al., “A review and evaluation of ballast settlement models using results from the Southampton Railway Testing Facility (SRTF)”, Procedia Engineering, 143: 999–1006, 2016.

[7] H.F. Lam, J.H. Yang, Q. Hu, et al., “Railway ballast damage detection by Markov chain Monte Carlo-based Bayesian method”, Structural Health Monitoring, 17(3): 706–724, 2018.

[8] L. Wang, M. Meguid, H.S. Mitri, “Impact of ballast fouling on the mechanical properties of railway ballast: insights from discrete element analysis”, Processes, 9(8): 1331, 2021.

[9] S.S. Artagan, V. Borecky, “Advances in the nondestructive condition assessment of railway ballast: a focus on GPR”, NDT & E International, 115: 102290, 2020.
[10] A. Benedetto, F. Tosti, L.B. Ciampoli, et al., “Railway ballast condition assessment using ground-penetrating radar–an experimental, numerical simulation and modelling development”, Construction and Building Materials, 140: 508–520, 2017.
[11] H. Cui, J. Li, Q. Mao, et al., “STSD: a large-scale benchmark for semantic segmentation of subway tunnel point cloud”, Tunnelling and Underground Space Technology, 150: 105829, 2024.
[12] A.M. Zarembski, J.W. Palese, T.L. Euston, “Correlating ballast volume deficit with the development of track geometry exceptions utilizing data science algorithm”, Transportation Infrastructure Geotechnology, 4(2): 37–51, 2017.
[13] J. Sadeghi, M.E.M. Najar, J.A. Zakeri, et al., “Development of railway ballast geometry index using automated measurement system”, Measurement, 138: 132–142, 2019.
[14] P. Lesiak, P. Bojarczak, A. Sokołowski, “Algorithm for the extraction of selected rail track ballast degradation using machine vision”, Transport Problems, 18, 2023.
[15] E. Aldao, H. González-Jorge, L.M. González-deSantos, et al., “Validation of solid-state LiDAR measurement system for ballast geometry monitoring in rail tracks”, Infrastructures, 8(4): 63, 2023.
[16] J. Luo, K. Ding, H. Huang, et al., “Towards automated field ballast condition evaluation: field validation of the ballast scanning vehicle capabilities”, Transportation Geotechnics, 48: 101311, 2024.
[17] P. Bojarczak, P. Lesiak, W. Nowakowski. “Automatic detection of ballast unevenness using deep neural network” Applied Sciences, 14(7): 2811, 2024.
[18] H. Cui, X. Ren, Q.Z. Mao, et al., “Shield subway tunnel deformation detection based on mobile laser scanning” Automation in Construction, 106: 102889, 2019.
[19] C.J. Dong, Q.Z. Mao, D.H. Kou, et al., “Dynamic precision surveying of railway tunnels based on MLS with robust constraints of track control network” Measurement Science and Technology, 33(8): 085015, 2022.
[20] Q.Z. Mao, H.X. Xu, J. Zhu, et al., “Immediate detection of over-under break of tunnel under construction using high-density point cloud”, Geomatics and Information Science of Wuhan University, 50(3), 562-570, 2025.
[21] T.T. Chen, M.H. Ran, T.G. Zhang, et al., “Detection methods for ballast supplement amount of newly-built railway lines based on MLS”, Geomatics and Spatial Information Technology, 47(12), 171-174,177, 2024.